Chapter 4

Memristive Systems Based on Two-Dimensional Materials

Gennady N. Panin and Olesya O. Kapitanova

Additional information is available at the end of the chapter

http://dx.doi.org/10.5772/intechopen.78973

Abstract

The unique electronic and optical properties of newly discovered 2D crystals such as graphene, graphene oxide, molybdenum disulfide, and so on demonstrate the tremendous potential in creating ultrahigh-density nano- and bioelectronics for innovative image recognition systems, storage and processing of big data. A new type of memristors with a floating photogate based on biocompatible graphene and other 2D crystals with extremely low power consumption and footprint is considered. The photocatalytic oxidation of graphene is proposed as an effective method of creating synapse-like 2D memristive devices with photoresistive switching for nonvolatile electronic memory of ultrahigh density. Particular attention is paid to the new concept of the formation of self-assembled nanoscale memristive elements interfacing artificial electronic neural networks. 2D photomemristors with a floating photogate exhibit multiple states controlled in a wide range of electromagnetic radiation and can be used for neuromorphic computations, pattern recognition and image processing needed to create artificial intelligence.

Keywords: 2D memristor, graphene, graphene oxide, molybdenum disulfide, resistive memory, photoresistive switching, photomemristor, artificial neural networks

1. Introduction

Memristive electronic systems, similar to biological synapses in neural networks, are a new type of electronic logic switches and memory with extremely low energy consumption and footprint. These new electronic components can solve the problem of physical and technological limitations of modern CMOS technology and create an elemental base for artificial intelligence. The unique electronic and optical properties of newly discovered atomic two-dimensional (2D) crystals, such as graphene, graphene oxide, molybdenum disulfide, and so

on demonstrate a huge potential for designing ultrahigh density nano- and bioelectronics for innovative information systems.

The chapter consists of the Introduction (Paragraph 1) and five sections that describe a brief history of the memristor and nonlinear effects in semiconductor electronics (Paragraph 2), the discovery of 2D crystals and a multilevel ultrafast nonvolatile memory based on graphene oxide (Paragraph 3), a memristor with a floating photogate (Paragraphs 3 and 4), a photonic chip with a photon synapse (Paragraph 5), a 2D TMD memory obtained on large-scale substrates (6) and Conclusion (Paragraph 7). Here we present a modern state of memristive systems, where signaling is analogous to signaling in biological neural networks. The focus is on 2D nonvolatile resistive memory based on molybdenum and graphene/graphene oxide (G/GO), which is biocompatible and allows the use of a neuromorphic architecture for analog computation and self-assembly technology. Photocatalytic and electron-beam oxidation-reduction of graphene/graphene oxide is considered as an effective method of manufacturing 2D memristors with photoresistive switching for nonvolatile memory of ultrahigh capacity. A new type of multifunctional memristor with a photogate, controlled electrically and optically over a wide range of wavelengths, can be used for image processing, pattern recognition and recognition of sounds, movements and speech needed to create artificial intelligence.

2. Memristor and nonlinear effects in solid state electronics

The definition of the memristor as a nonlinear resistive element was introduced by Leon Chua in 1971 to describe the missing fourth base element of the electrical circuit [1]. The memristor, along with other known circuit elements, such as a capacitor, a resistor and an inductor, could describe nonlinear effects in solid state electronics that were already well known. In 1922, Oleg Losev observed a new phenomenon of negative differential resistance in a two-electrode point device—a cristadyne [2, 3]—which was then used to generate and detect a signal for radio broadcasting around the world. Losev's cristadyne allowed to work at frequencies up to 100 MHz, at that time not conceivable and not understandable for applications. Later, Oleg Losev improved his cristadyne, adding to it a third electrode, which could control the current in this device. The article on the new nonlinear three-electrode device, sent by Losev to the "Physical Review" in 1942 from besieged Leningrad was lost and not published. The great interest in this topic was also in other laboratories. In 1948, John Bardeen of Bell Labs received a patent for a point-contact three-electrode element [4] and, together with Walter Brattein, described the physical principles of the transistor effect [5–9]. In 1956, for the discovery of the transistor effect, William Shockley, John Bardeen and Walter Brattein received the Nobel Prize in Physics. In 1957, Leo Esaki demonstrated independently a similar nonlinear device—a tunnel diode—and in 1973 received for the discovery of this effect the Nobel Prize in Physics.

Interest in the nonlinear two-electrode memristive device increased sharply in 2008, when the memristor was detected experimentally in the HP laboratory [10]. This device consisted of two nanoscale regions, doped and undoped, the relative displacement of which controlled

http://dx.doi.org/10.5772/intechopen.78973

the on and off states. The first matrix of memristors was made on the basis of TiO_2 on a CMOS chip in the HP laboratory in 2012. A memristor with two platinum electrodes was a nonlinear dynamic structure whose resistance depended on the electric field and the current flow (**Figure 1**). This nonlinear device made it possible to form nonvolatile states that allow storing information with the power supply off, had the ability to obtain ultrahigh recording density, low switching energy, high operating speed, long storage time and the possibility of multilevel recording using discrete or continuous states.

The memristor is a memory resistor with variable resistance and is described by the conductivity depending on the flux and field. In 2016, Fujitsu Semiconductor and Panasonic Semiconductor demonstrated the first serial product of 4 Mb RRAM. Using a nonlinear dynamic approach allows you to effectively solve a number of complex computational problems for image processing and pattern recognition. For example, a commercial product Toshiba Smart Photo Sensor with a universal chip based on a cellular neural network (CNN) is capable of processing images, similar to the human brain, which allows to calculate the elementary problems of image recognition within nanoseconds. It was shown that the CNN chip is so fast that it can detect a bullet in flight and have enough time to program another bullet in order to knock it down.

Memristors, which are similar to synapses in biological neural networks, can become an elemental base for creating high-performance intelligent machines and computers with a neuromorphic architecture similar to the brain. It is known that the human brain, containing 10^{10} neurons and 10^{14} synapses (**Figure 2**), processes analog information and consumes only about 20 Watts. A modern supercomputer with digital processing of information to simulate the operation of a neural network of only 1% of the number of neurons of the human brain requires about 10^6 Watts. To simulate the work of the human brain within 1 s, the supercomputer "K Computer" (up to 10 petaflops, 10^{16} billion operations per second, 1 petabyte of RAM)—the development of the Japanese corporation "Fujitsu"—takes about 40 min. Thus, an analog processor based on a neuromorphic memory system is much more efficient than a modern digital supercomputer. The key moment of this system is special processes of signal transmission in neural networks, which are paid great attention to by researchers. In 2000, the Nobel Prize in Physiology was awarded to Arvid Karlsson, Paul Gringard and Erik R. Kandell for "discoveries in the transmission of signals in the nervous system." Neural networks have

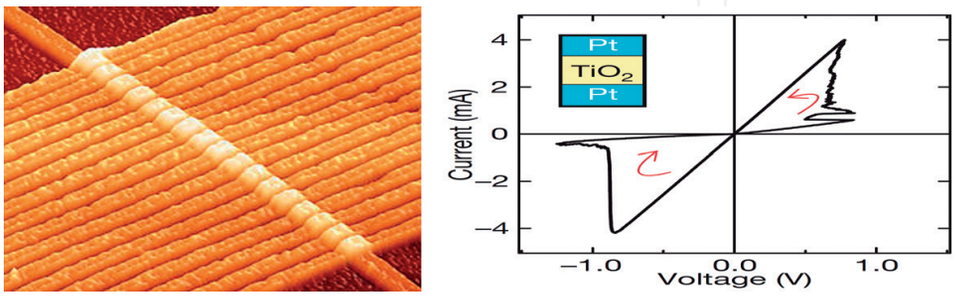

Figure 1. Memristors on CMOS chip (HP 2012) and the I/V-characteristic of $Pt/TiO_2/Pt$ memristor.

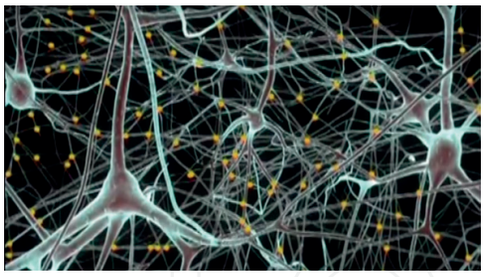

Figure 2. Neural network.

associative memory and the ability to learn deeply, the knowledge of which was laid down in the works of the Russian physiologist Ivan Pavlov, who received the Nobel Prize in Physiology in 1904. The study of digestion pushed him to the idea of conditioned reflexes. Such acquired reflexes arise under certain conditions and disappear when conditions are not observed.

3. Atomic 2D graphene crystal

Graphene is a crystalline two-dimensional layer of carbon with the thickness of one atom (**Figure 3**). A huge interest in this material appeared in 2004 after the joint publication of researchers from IMT RAS and Manchester University on the effect of an electric field in atomic-thin carbon films [11]. Six years later in 2010, Andrei Geim and Konstantin Novoselov were awarded the Nobel Prize in Physics for "pioneering experiments with 2D graphene material."

Graphene consists of two symmetric carbon sublattices that form the Dirac cone of the linear energy dispersion of the electrons, which are called Dirac fermions. The peculiarity of these particles is that they are massless and behave like photons. In consequence, graphene demonstrates magical properties. Graphene transparent (97.7%), resistant to an extremely high current density (one million times higher than that of copper), has the highest electron mobility of known materials (~10^6 cm^2 B^{-1} s^{-1}, three orders of magnitude higher than in silicon) and a very high thermal conductivity ($K > 5 \times 10^3$ $W/(m \times K)$), which is higher than that of a diamond. Graphene is a well stretchable (25%) material with a unique mechanical strength $E > 10^{12}$ Pa (six times higher than steel). In addition, graphene shows very good biocompatibility.

3.1. Memristor based on graphene/graphene oxide

In 2010, researchers from IMT RAS and Dongguk University demonstrated a graphene/graphene oxide (G/GO) memristor that switched at 0.7 V and 1 nA, with an on/off ratio of about 10^3 (**Figure 4**) [12, 13]. The electron beam-induced current method made it possible to reveal, with a high spatial resolution, the formation of randomly distributed current filaments (**Figure 5**) and to study the switching mechanism in this device like a synapse. The resistance of this device varied nonlinearly in the electric field, and the values of high and low resistance were nonvolatile.

http://dx.doi.org/10.5772/intechopen.78973

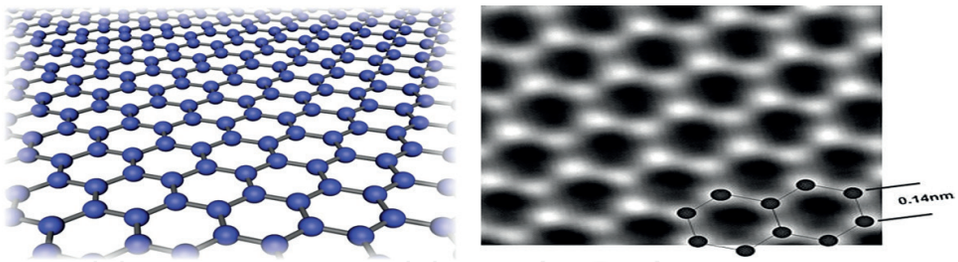

Figure 3. The crystal lattice of graphene.

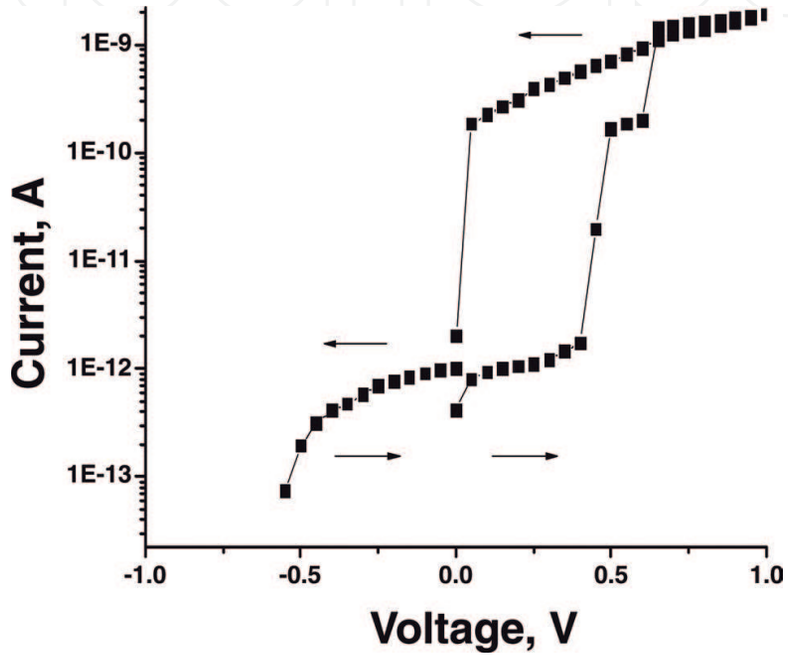

Figure 4. Resistive switching of the Al/GO/Al structure, performed at 5 V [12].

3.2. The mechanism of resistive switching in graphene/graphene oxide

The mechanism of resistive switching in G/GO was studied in detail in a number of works [12–17] in which it was shown that the migration of oxygen-containing groups in GO plays an important role. One sp^3 carbon-oxygen or carbon-hydroxyl bond on 10^6 sp^2 bonds reduced conductivity in carbon nanomaterials by 50% [18]. Graphene oxide with a sp^3 carbon configuration possessing low electrical conductivity was switched in an electric field locally in the sp^2 configuration of carbon (**Figure 6**), which led to high electrical conductivity. This process can be controlled both by adsorption/desorption of oxygen and by migration of oxygen-related groups.

3.3. Self-organization of memristors based on graphene/graphene oxide

The photocatalytic oxidation of graphene coated with a layer of 10–15 nm ZnO nanoparticles under ultraviolet (UV) irradiation conditions led to the formation of self-organized G/GO memristors with very high density (10^{12} cm^{-2}) [16, 17]. **Figure 7** shows the scheme of photocatalytic oxidation of graphene with ZnO nanoparticles. A 2–3-layer graphene coated with

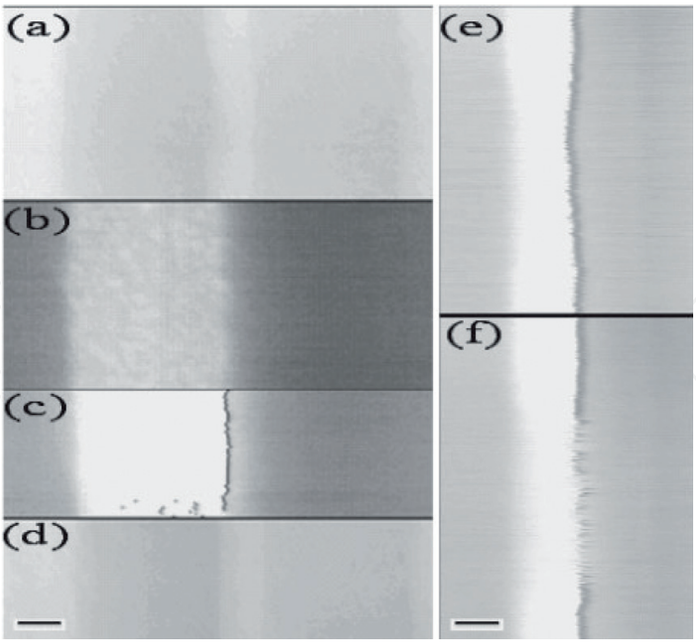

Figure 5. Scanning electron microscope (SEM)-remote induced current (REBIC) images of the Al/GO/Al structure with the modulation of the built-in potential barrier near the negatively biased Al electrode at different bias (V_b) and forming (V_f) voltages. (a) $V_b = 0$; $V_f = 0$ (SE mode); (b) $V_b = 0$; $V_f = 0$ (REBIC mode); (c) $V_b = 0$; $V_f = 5$ V (REBIC mode); (d) $V_b = 0$; $V_f = 5$ V (SE mode); (e) $V_b = 0.2$ V; $V_f = 7$ V (REBIC mode); (f) $V_b = 0.5$ V; $V_f = 7$ V (REBIC mode, same area as in (e)). A scale mark of 100 μm (e) and (f), 50 μm in (a)–(d). The images in (a)–(d) were obtained by sequentially switching signals of secondary electrons (SE) and remote induced current (REBIC) during scanning of the electron beam [12].

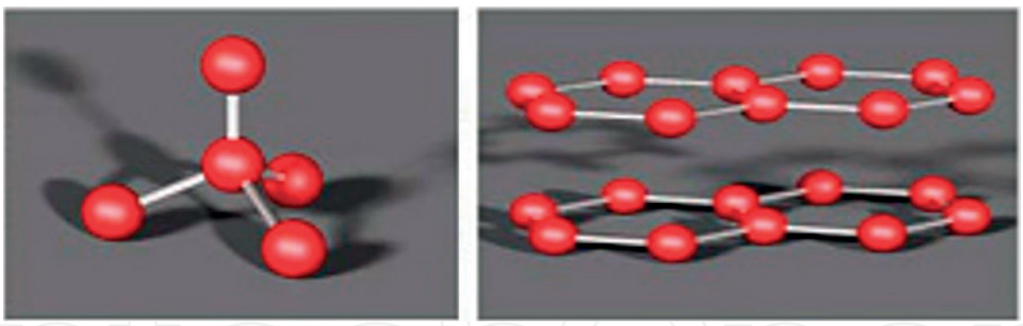

Figure 6. sp^3 (left) and sp^2 (right) of the carbon configuration.

particles was irradiated in a moist air stream at room temperature or above (80°C) using a quartz UV lamp with a light flux of 0.03 J $min^{-1} \times cm^2$. Light with a wavelength exceeding 365 nm was filtered. The time of ultraviolet irradiation ranged from 5 to 90 min. After ultraviolet treatment, the ZnO nanoparticles were dissolved in dilute 0.1 M HCl, the graphene substrate was washed with deionized water and dried in nitrogen.

ZnO nanoparticles play a key role in the process of photooxidation of graphene. **Figure 8** shows the electronic diagram of graphene/ZnO interface under UV irradiation. The bending of the bands upward in the ZnO nanoparticles is caused by a lower electron work function in ZnO (3.6 eV) compared to graphene (4.5 eV). Electron–hole pairs generated in ZnO (3.3 eV) under UV irradiation (reaction 1) are separated in a built-in electric field at the graphene/ZnO

http://dx.doi.org/10.5772/intechopen.78973

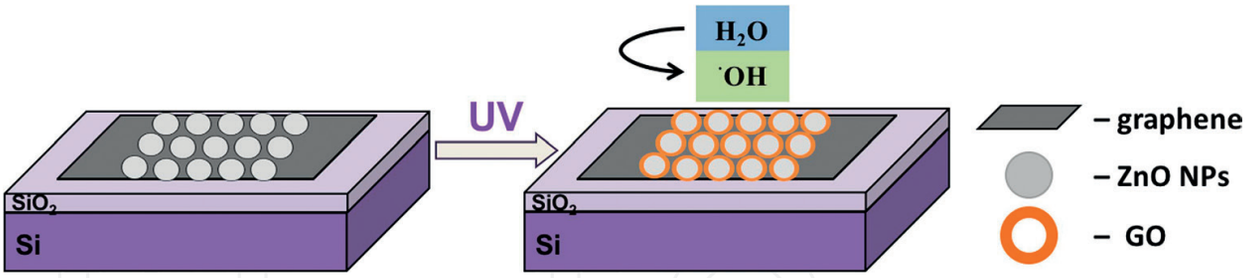

Figure 7. Scheme of photocatalytic oxidation of graphene coated with ZnO nanoparticles under UV light to form G/GO heterostructures on a Si/SiO_2 substrate [17].

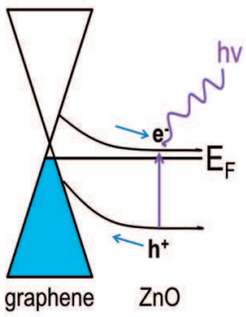

$$ZnO + h\nu \rightarrow ZnO(h^+ + e^-)_{3.3eV} \quad (1)$$

$$2h^+_{3.3eV} + H_2O \rightarrow 2H^+ + O_2 \quad (2)$$

$$2e^-_{3.3eV} + O_2 \rightarrow O_2^- \quad (3)$$

$$O_2^- + 2H^+ \rightarrow H_2O_2 \quad (4)$$

$$H_2O_2 + h\nu \rightarrow 2\cdot OH \quad (5)$$

Figure 8. Schematic electronic diagram of the G/ZnO interface under UV irradiation. Electron-hole pairs generated in ZnO (3.3 eV) under UV irradiation (reaction 1) are separated in a built-in electric field at the G/ZnO interface, providing a flux of holes to graphene [16].

interface, which provides a hole flux (3.3 eV) to graphene. As a result, graphene is decorated with highly reactive hydroxyl radicals (· OH) through O_2^- and H_2O_2 (reactions 3–5) processes of photodecomposition of water molecules from moist air.

3.4. Memristors based on graphene with a floating gate of ultrahigh density

Controlling the distribution of ZnO nanoparticles on graphene with a well reproducible size (10–15 nm) makes it possible to create highly scalable nanoheterojunctions of G/GO for ultra-high-density memory (up to 10^{12} cm^{-2} or 1 Tb on a chip for the vertical geometry of crossing electrodes, **Figure 9**).

Memristors with a floating photogate are electrically read with or without optical excitation. The I-V curve of the graphene sample before oxidation demonstrates linear behavior and high conductivity of graphene (**Figure 10(a)**, black curve). The photocatalytic process leads to a decrease in current through the sample by two orders of magnitude and a nonlinear behavior indicating the formation of a bandgap in the oxidized graphene (**Figure 10(a)**, red curve).

The rise in the temperature of moist air reduces the oxidation time of graphene. The G/GO heterostructures obtained by photocatalytic oxidation by blowing moist air at room temperature for 30 min and at 80°C for 5 min demonstrate a nonlinear behavior with a GO band width of about 3 eV, which reduces the conductivity of oxidized graphene by two orders of magnitude compared to graphene. The formed G/GO nanostructures demonstrated good

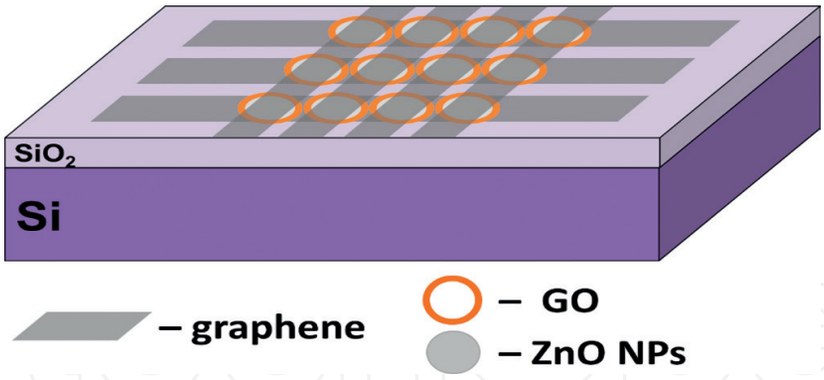

Figure 9. Scheme of arrays of G/GO photomemristors in vertical geometry obtained by photocatalytic oxidation of graphene with ZnO nanoparticles [17].

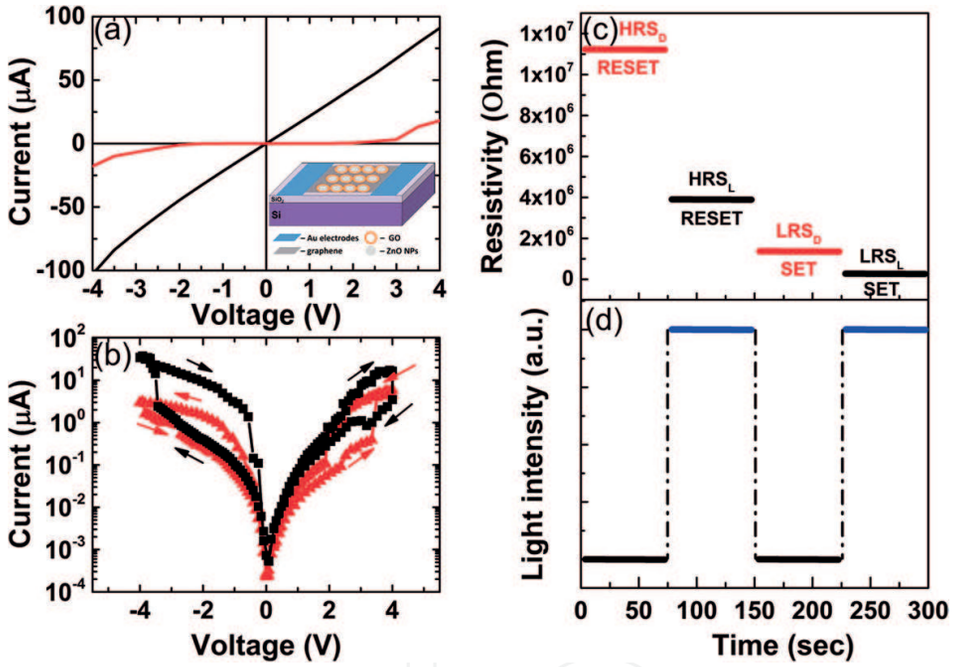

Figure 10. (a) I-V characteristics of the 2–3 layer G/ZnO structure before (black) and after (red) photocatalytic oxidation in moist air for 30 min at room temperature. Insert-scheme for measuring the structure with lateral gold electrodes. (b) I-V characteristics for the G/GO nanostructure preliminarily polarized (+5 V, 15 min) with white light (black) and in the dark (red). (c) Resistive states of the G/GO photomemristor, which are switched by a voltage of −3.8/3.3 V (Reset/Set) in the dark and −3.5/4 V (Set/Reset) under white light pulses (d) and read at 2.5 V [17].

photosensitivity to white light and photoresistive switching. The photocurrent increased approximately six times at a bias voltage greater than 3 V. This indicates that the electron–hole pairs generated by light are effectively separated in the biased G/GO heterojunctions. **Figure 10(b)** shows the I-V characteristics of the preformed G/GO nanostructure (+5 V, 15 min) when sweep voltage of −4 to 4 V under white light (black) and in the dark (red). Well reproducible bipolar hysteresis indicates a resistive switching of the structure with an on/off ratio of about 10 for 4 different resistive states HRSD, LRSD, LRSL and HRSL in the dark and light with switching voltages of −3.8/3.3 V (Reset/Set) and −3.5/4 V (Set/Reset), respectively (**Figure 10(c)** and **(d)**). To form vertical memristive structures, ZnO nanorods (NR) grown on graphene can also be used instead of ZnO nanoparticles (**Figure 11**) [16].

The vertical structure of the G/GO/ZnO nanorods (NR) allows selective excitation with UV light of 380 nm. Resistive switching in heterostructures of G/GO/ZnO NR was observed at voltages <1 V with the ratio of high/low resistance of 10^3 after the forming process at 1 V (**Figure 12(b)**).

The structure of resistive memory based on graphene and ZnO NR is promising for memristive devices with high density and low power consumption.

3.5. Graphene/graphene oxide memristors formed by an electron beam

Electron beam annealing GO stimulates a radical mechanism for the reduction of GO due to the formation of hot electrons. These electrons destroy the weak C-O and C-H bonds (in comparison with strong C-C bonds) and form highly reactive radicals $O^{\cdot}$ and $H^{\cdot}$, which

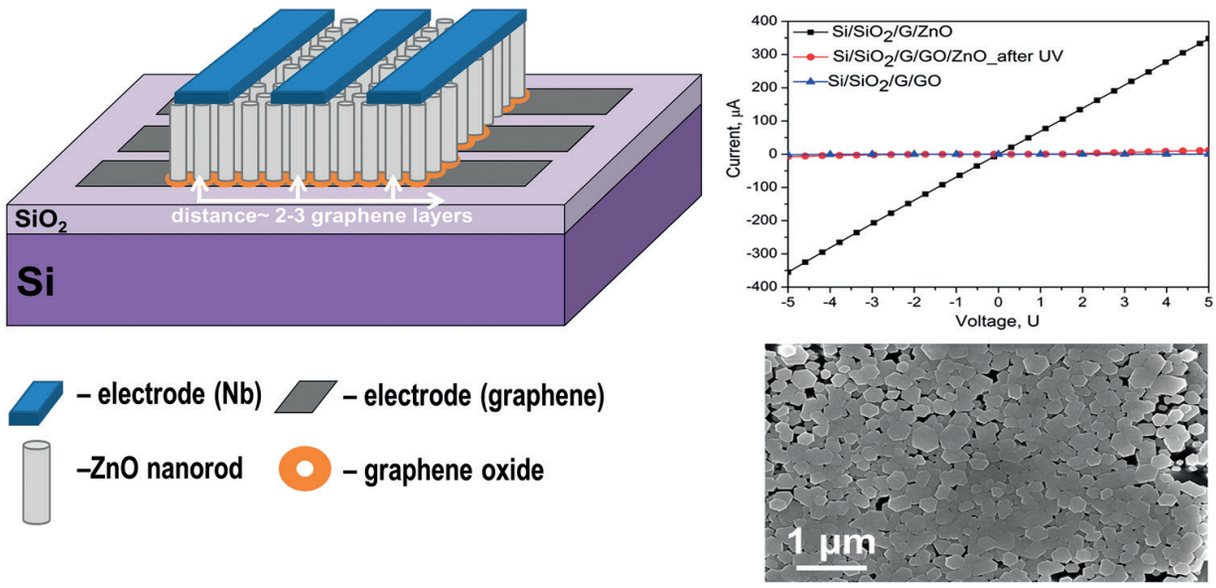

Figure 11. Scheme of arrays of G/GO/ZnO NR photomemristors in vertical geometry (left) and a SEM image of the structure (lower right) with their current-voltage characteristics (upper right) [16].

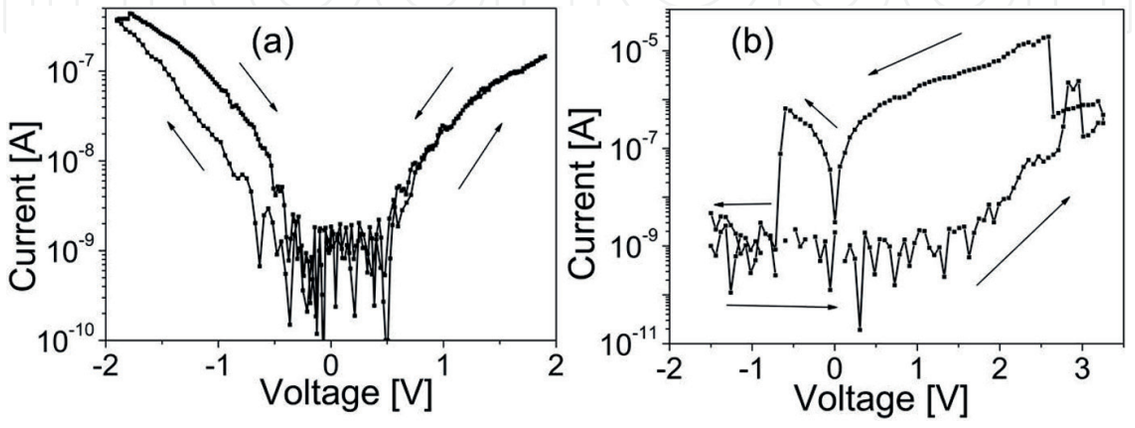

Figure 12. I-V characteristics of the vertical structure G/GO/ZnO in a semilogarithmic scale (a) without forming and (b) after the forming process [16].

recombine in H_2O, H_2, O_2, and the uncompensated charge in GO is used to restore the sp^2 carbon bond. It should be noted that the electron beam annealing process excites the electronic subsystem selectively, and the energy of the generated hot electrons can be resonantly absorbed by the functional groups of graphene oxide. To remove oxygen groups, several eV are required, which is comparable to the energy between orbitals. Primary beam electrons are high-energy and can participate in annealing only through the process of energy absorption by graphene oxide to form hot electrons with an energy close to the GO bandgap (E_g). Electron-stimulated annealing of GO can occur due to the generation of a high concentration of charge carriers in this material (E_g = 1–6 eV) (an electron beam with an electron energy of 3–10 keV creates 10^3 electron-hole pairs per incident electron). The process of electron-stimulated annealing by an electron beam is more effective than laser annealing, in which one photon produces only one electron-hole pair, and therefore the thermal effects in laser annealing make the main contribution. Electron beam annealing allows the direct formation of rGO/GO memristive nanostructures with controlled reduction without the use of a mask. **Figure 13** shows a SEM image of a GO film with a superimposed stripe pattern (green) for electron-beam exposure (a) and a rGO/GO/rGO structure obtained by direct "writing" by an electron beam with a dose of 150 mA × s/cm^2 (b, c). The change in image contrast in the secondary electron emission (SEE) of graphene oxide after electron beam processing (b, c) indicates a change in composition and its electronic properties.

The electron beam annealing of GO allows for more efficient formation of a resistive switching structure. The lateral structure of rGO/GO/rGO obtained by electron beam irradiation with a dose of 200 mA × s/cm^2 exhibited soft resistive switching without the forming process. The curve of the I-V structure, after irradiation, was nonlinear with a small hysteresis

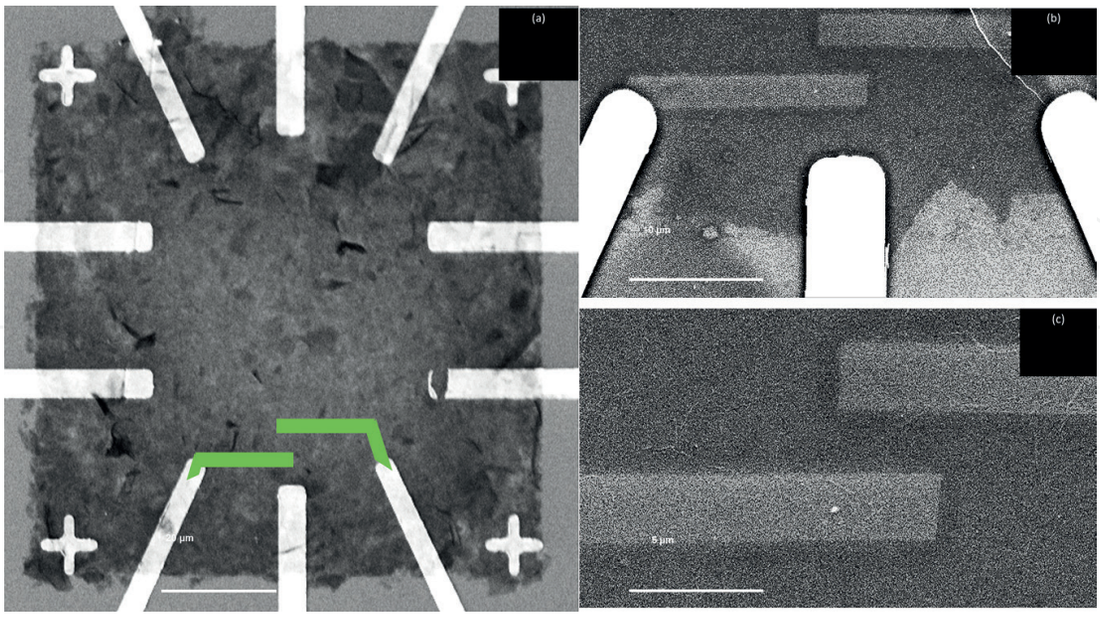

Figure 13. SEM images of a GO film on a SiO_2/Si substrate with Pt electrodes (white) and superimposed stripe pattern (green) for electron beam writing (a) and rGO/GO/rGO structure after irradiation with an electron beam (b, c). The narrow bands of the brighter SEE contrast are regions of the reduced rGO after irradiation.

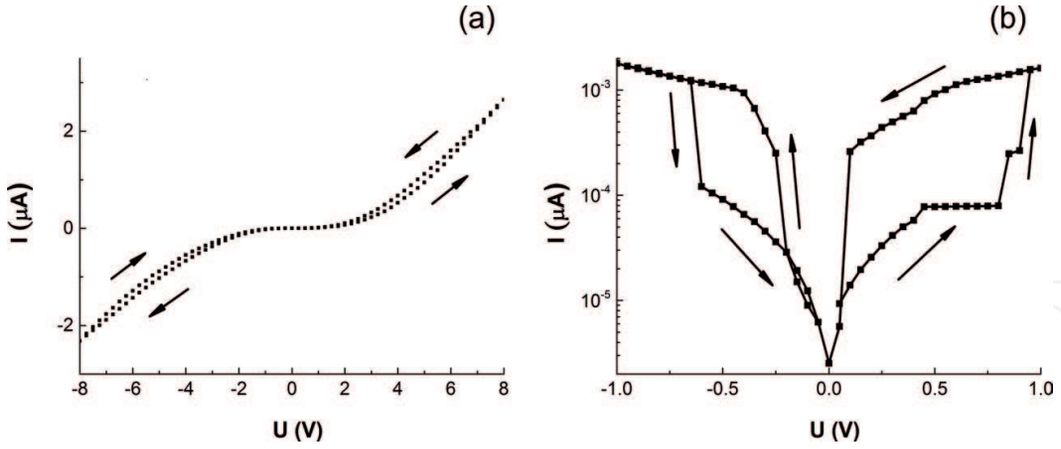

Figure 14. I-V characteristics of the Pt/GO/Pt structure after electron irradiation before (a) and after (b) the forming process.

(**Figure 14(a)**). The forming process at 20 V led to an increase in the conductivity of the structure by several orders of magnitude and to a pronounced nonlinearity. A bipolar hysteresis was observed that indicated a resistive switching of the structure from the high-resistive resistive state (HRS) ((1.2 ± 0.1) × 10^{11} Ω) to the low-resistive resistive state (LRS) ((6.7 ± 0.4) × 10^{8} Ohm) (~2 orders of magnitude) at a low switching voltage of 0.8–0.9 V (**Figure 14(b)**). The electron beam annealed structures showed good reproducibility with a small spread of switching voltages (0.05–0.1 V).

3.6. Multilevel ultrafast nonvolatile memory based on graphene oxide

Memory with the ability to store more than one bit per cell, that is, having multilevel memory states, is very attractive, since it offers a simple and economical way to increased memory capacity (e.g., modern CMOS NAND-Flash usually stores 2 or 3 bits per cell). Combining this capability with tiered storage with extremely high scalability is especially effective for implementing memory with ultrahigh storage volumes. Access to four very well-separated and stable memory states in nanoscale GO cells by monitoring the duration and amplitude of the write pulse was recently demonstrated at IBM [19]. Excitation pulses with amplitudes from 2 to 6 V and duration from 20 to 80 ns were used to determine the conditions for successful recording and erasing of multilevel memory states in Pt/GO/Ti/Pt and monitoring of the resulting cell resistance, see **Figure 15(a)** and **(b)**.

The cells were completely switched from the RESET state, which can be considered as state 00 to memory states 01, 10 and 11 using pulses of −2.5 V/60 ns, −3.5 V/60 ns and − 4.5 V/60 ns respectively (**Figure 15(a)**). Erasing of cells from 01, 10 and 11 states back to state 00 was successfully achieved for pulses +3 V/60 ns, +4 V/60 ns and +5 V/60 ns, respectively (**Figure 15(b)**). Separation of intermediate resistance levels is very good (see **Figure 15(a)**), which allows a reliable reading process. Intermediate levels showed excellent reliability (**Figure 15(c)**) and were stable over time (**Figure 15(d)**), both on rigid and flexible substrates. The reversible resistive switching observed in these devices was due to the migration of oxygen, which led to a change in the conductivity.

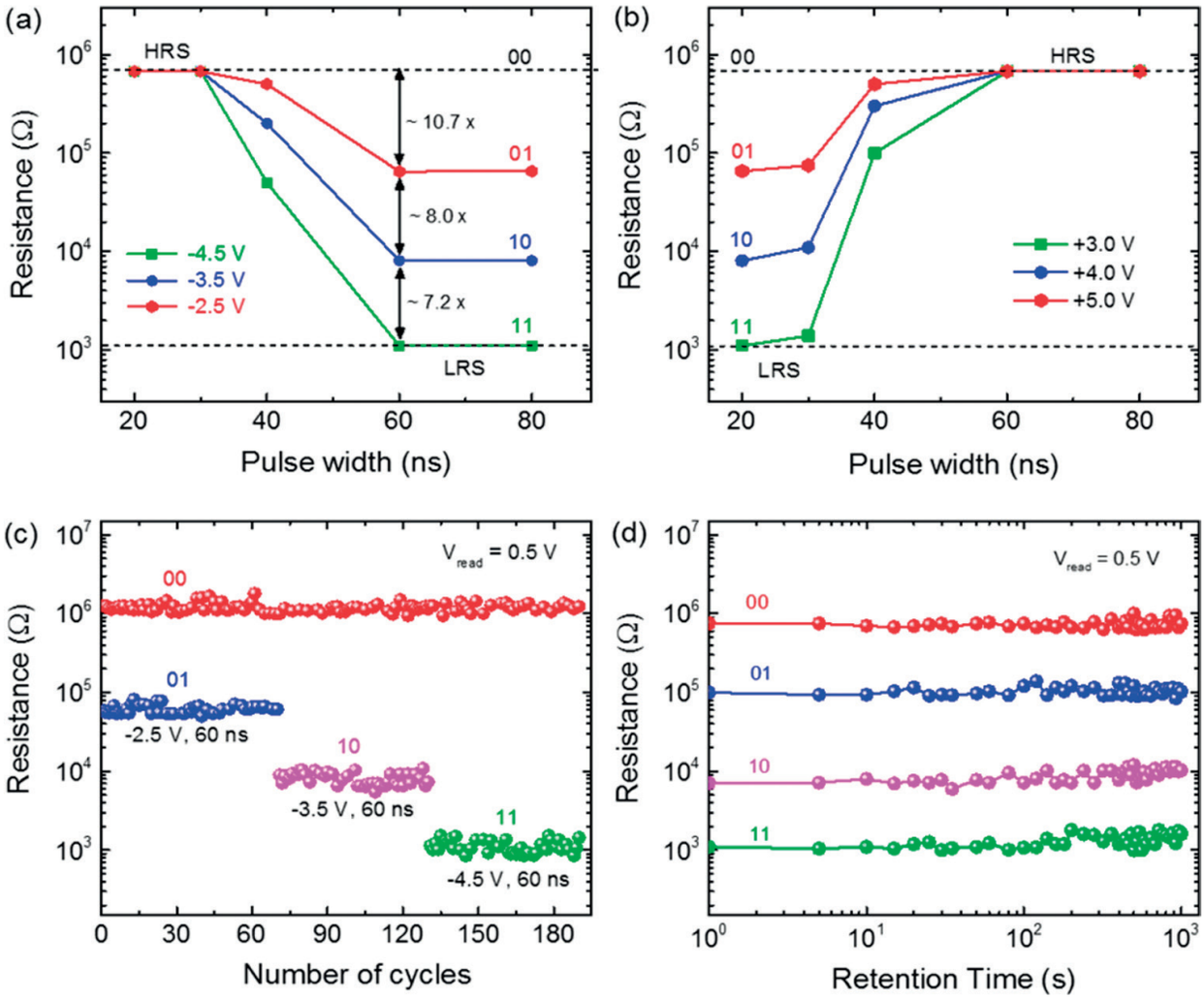

Figure 15. (a) Record and (b) erase multilevel states in a 75 nm GO memory cell (8 nm-thick GO layer) by controlling the amplitude and pulse width. (c) reliability and (d) storage of states of a multilevel, nanoscale graphene oxide cell [19].

4. Memristor with floating MoS_2 photogate

A memristor with a floating MoS_2 photogate polarized in an electric field under different lighting conditions demonstrates a multilevel switching [20]. **Figure 16** shows the current–voltage curves (I-V) of the Au/MoS_2/Au structure (an inset in **Figure 16(a)**) after polarization at 3 and 6 V. The nonlinear characteristics of a device with hysteresis indicate a memristive behavior. Furthermore, the memristor demonstrates a high photoresponse when illuminated with white light. When the device is polarized at 3 V, a smooth switching from HRSL3 to LRSL3 is observed under light illumination and from HRSD3 to LRSD3 in the dark with a ratio of on/off currents of about 2 and 4 at 1.2 V and 0.7 V, respectively (**Figure 16(a)**). At a higher voltage (6 V), the device shows a sharp switching when excited by white light, from HRSL6 to LRSL6 at −2.9 V with an on/off ratio of about 10 and a smooth switching from HRSD6 to LRSD6 in the dark with an on/off ratio of about 3 at 0.7 V (the SET process of

writing the ON state, **Figure 16(b)**). When the applied voltage changes from 0 to positive voltage (4.2 V), the device returns to HRSL6 (RESET operation to clear the state ON to OFF). The memristive behavior of the device in darkness and in light is well reproduced up to 1000 cycles (**Figure 16(c)** and **(d)**) and demonstrates the possibility of obtaining in the device a multilevel resistive switching and its control by means of an electric field in the dark and when excited by light.

It should be noted that resistive switching controlled by the polarization of MoS_2 nanospheres is a faster process than ion transport, and the frequency of optical access is much higher than electrical addressing.

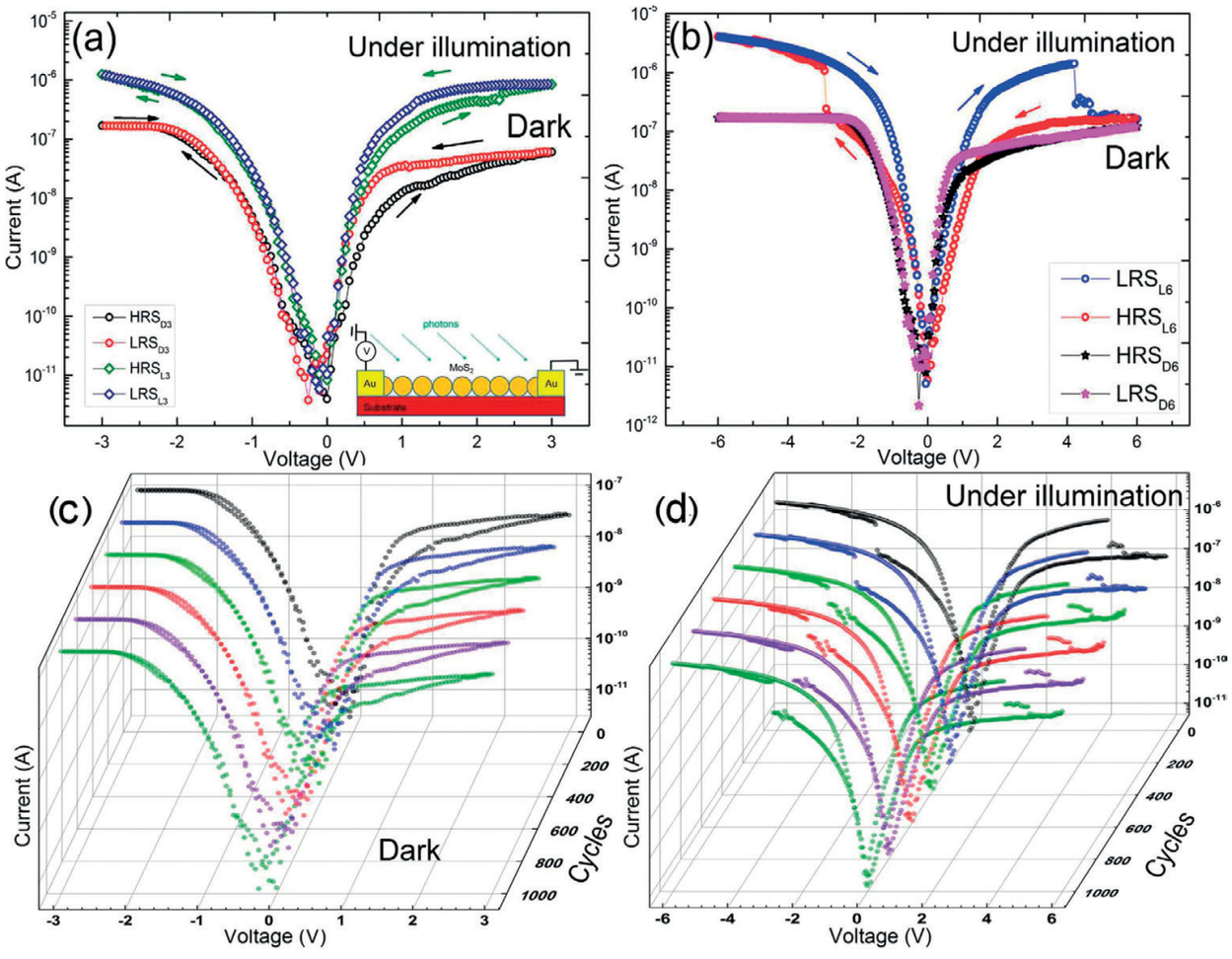

Figure 16. Resistive switching of the nanospheric photomemristor Au/MoS_2/Au. I-V characteristics in the dark or under white light (spectral maxima at 2.7 eV and 1.8 eV; device diagram on the inset in **Figure 16(a)** with light excitation). The arrows on the curves indicate the direction of the voltage sweep; (a) I-V curves after 3 V voltage polarization. The device smoothly switches from HRSL3 to LRSL3 under light and from HRSD3 to LRSD3 in the dark with an on/off ratio of about 2 and 4 at 1.2 V and 0.7 V, respectively; (b) I-V curves after a 6 V voltage polarization. The device shows abrupt changeover of resistance when excited by light, from HRSL6 to LRSL6 at −9.2 V with an on/off ratio of about 10 and a smooth transition from HRSD6 to LRSD6 without light excitation with a switching factor on/off about 3 at 0.7 V. (c) Memristive characteristics of the device without excitation by light after several cycles. (d) Memristive characteristics of the device when excited by white light after several cycles [20].

4.1. 8-Level memristor system with an MoS_2 floating photogate

The diagram of the operation of the 8-level memristor system with the MoS_2 floating photodetector is shown in **Figure 17**, where the resistance states formed after the SET/RESET operation of the MoS_2 memristor polarized at voltages of 3 V and 6 V in the dark or when excited by light are shown. A memristor polarized at 3 V in darkness or in white light demonstrates four states that are read at a voltage of 0.7 V (HRSD3 and LRSD3) and 1.2 V (HRSL3 and LRSL3) in the dark or in white light (**Figure 17(a)**).

Polarization of the memristor at 6 V in darkness or under light leads to the formation of four more states that are read at a voltage of 0.7 V (HRSD6 and LRSD6) and 4 V (HRSL6 and

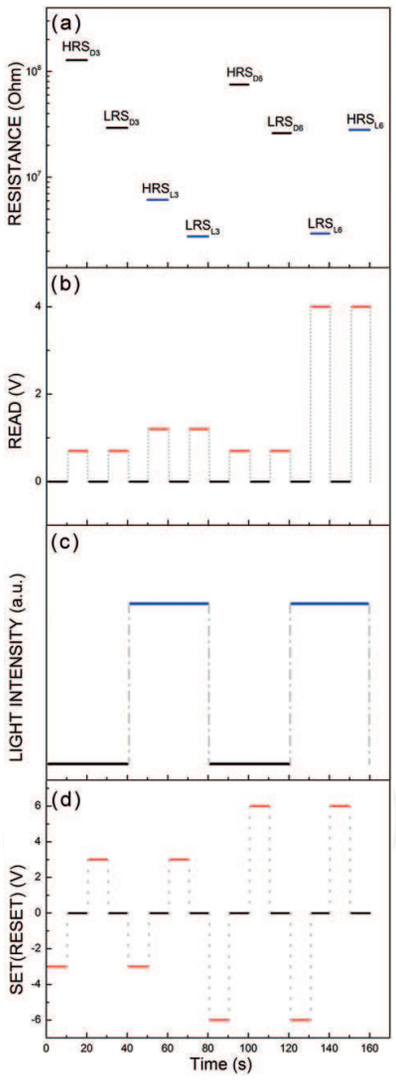

Figure 17. The operation of the MoS_2 photomemristor, polarized at different voltages in the dark or when excited by light. (1) high and low resistive states obtained using SET/RESET operations at −3 V/3 V and −6 V/+6 V in the dark (HRSD3, LRSD3 and HRSD6, LRSD6) and under white light (HRSL3, LRSL3, LRSL6 and HRSL6). (2) reading diagram under impulse voltage. Resistive states are read at 0.7 V (HRSD3, LRSD3, HRSD6 and LRSD6), 1.2 V (HRSL3 and LRSL3) and 4 V (LRSL6 and HRSL6) in dark (D) or white light (L). (3) excitation scheme by pulses of white light. SET/RESET and the READ operation is controlled by switching off the light pulses (black) (HRSD3, LRSD3, HRSD6 and LRSD6) and turned on (blue) (HRSL3, LRSL3, HRSL6 and LRSL6). A 3 V polarized memristor demonstrates four states that are read as HRSD3, LRSD3, HRSL3 and LRSL3, while a memristor polarized at 6 V demonstrates the other four states: HRSD6, LRSD6, HRSL6 and LRSL6, which can be read in the dark or in the light [20].

LRSL6) in darkness or in light (**Figure 17(a)**). These states are controlled electrically and optically, which is confirmed by the iterative operation of the memristor under various conditions of writing and reading (**Figure 17(c)** and **(d)**) Polarization of nanospheres in a photomemristor using an electric field and light pulses creates multilevel states. An analysis of the conductivity in these states of resistance shows that the polarization of nanospheres when excited by light leads to the formation of conductive paths. Reducing the gap between the electrodes can greatly minimize the operating voltage of the device. Modulation of the barrier height at the boundaries of the nanospheres in an external electric field by light due to repolarization is a highly efficient process for high-speed signal processing. The memristor polarized at 3 V and 6 V has different states that can be electrically read at optical excitation in the form of four high-resistance states and four low-resistance states. The optical and electrical polarization of the memristor provides several nonlinear dynamic processes that allow us to build a system with a neuromorphic architecture, similar to a neural network.

5. Photonic chip with photon synapse

A photonic chip containing 70 photon synapses was demonstrated in 2017 by a team from the universities of Oxford, Münster and Exeter [21]. The recording, erasure and reading of information in this case are carried out completely by optical methods (**Figure 18**). The photon synapse consists of a cone-shaped waveguide (dark blue) with discrete islands of phase-change

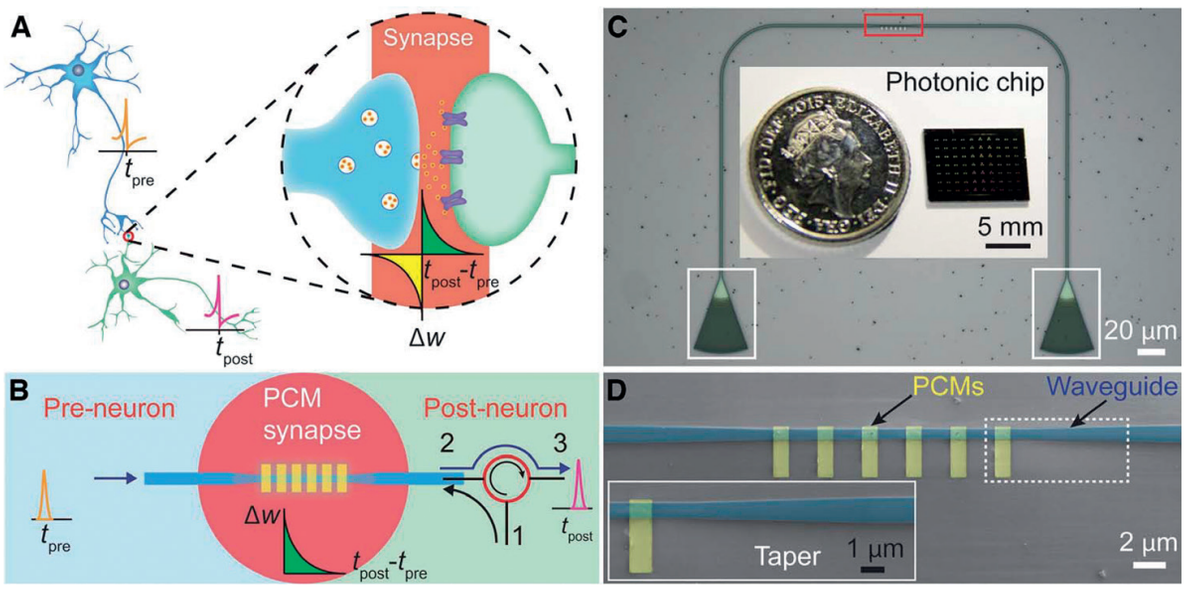

Figure 18. Photon synapse on a crystal. (A) The structure of the neuron and the synapse. Insert: Illustration of the synapse junction. (B) Scheme of the integrated photon synapse resembling the function of a neural synapse. The synapse is based on a cone-shaped waveguide (dark blue) with discrete PCM islands from the top, optically connecting presynaptic (preneural) and postsynaptic (postneural) signals. The red open circle is a circulator with port 2 and port 3, connecting the synapse and postneuron; weighing pulses are fed through port 1 to the synapse. (C) An optical microscope image of a device with an active region (red rectangle) as a photon synapse. The optical input and output of the device is carried out through apodized diffraction couplers (white rectangles). Box: A typical photonic chip containing 70 photon synapses is smaller than a coin. (D) Scanning electron microscope image of the photon synapse active region corresponding to the red rectangle in (C) with six $Ge_2Sb_2Te_5$ (GST) strips (1 × 3 μm, yellow) at the tip of the waveguide (blue). Insert: An increased conical waveguide structure, marked with a white dotted frame [21].

material (PCM) from the top optically connecting the presynaptic (preneuronal) and postsynaptic (postneuronal) signals. The use of purely optical means provides ultrafast operation speed, virtually unlimited bandwidth and no loss of electrical power on interconnects. It is significant that the synaptic weight can be randomly installed simply by changing the number of optical pulses that create a system with continuously changing synaptic plasticity, reflecting the true analog nature of the biological synapses.

5.1. Synaptic weight and plasticity

Synaptic adjustment of the device when switching between crystalline and amorphous states of GST islands with a recorded change in the relative transmission coefficient is shown in **Figure 19**. Five weight states of the photon synapse are obtained by switching the energy of the optical pulse (404.5 pJ, 50 ns). The photon synapse demonstrates good reproducibility of weight numbers with cyclic measurements (**Figure 19(B)**). In this case, the photon synaptic weight is determined by the number of optical pulses (**Figure 19(C)**).

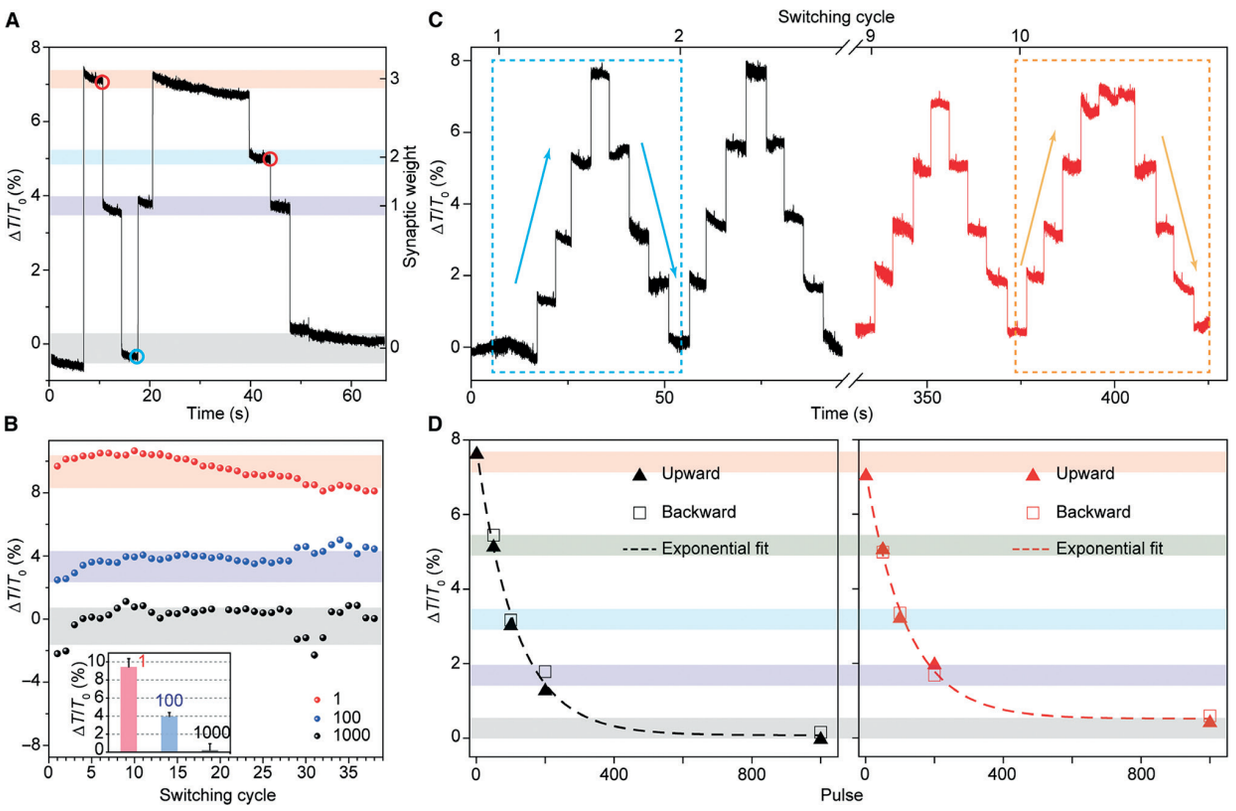

Figure 19. Synaptic weight and plasticity. (A) Demonstration of the differential synaptic weight of the device in **Figure 18** when switching between crystalline and amorphous GST island states with recorded relative coefficient change ($\Delta T/T_o$). Each weight can be achieved with the same number of pulses (50 ns at 243 pJ, 1 MHz) from any previous weight. (B) Weight repeatability for several cycles. Box: Statistical analysis of the change in readings for the weight "0," "1" and "4". The applied pulse was 50 ps at 320 pJ, slightly larger than in (A). (C) Five weights of the photon synapse are obtained when the energy of the optical pulse is switched (404.5 pJ, 50 ns). Dotted blue (yellow) rectangles correspond to the first (last) weight cycle. The up and down arrows in the rectangles are the weighing directions. (D) Photon synaptic weight ($\Delta T/T_o$) as a function of the number of optical pulses. The left (right) panel corresponds to the data of the marked blue (yellow) field in (C). Painted triangles (not filled squares) represent data from the upward (downward) direction of weighing. The dashed lines represent the exponential curves closest to the experimental data [21].

6. 2D Transition metal dichalcogenides (MoS_2, $MoSe_2$, WS_2 and WSe_2) memory

MOCVD growth of semiconductor monolayer MoS_2 films and tungsten disulfide (WS_2) on silicon oxide at 500°C on a 4-inch wafer allows to obtain excellent electrical characteristics and structure for 2D memristors (**Figure 20**).

6.1. Atomistor: nonvolatile atomic resistive TMD memory

In 2017, the Argonne National Laboratory demonstrated an atomistor: a nonvolatile atomic resistive 2D TMD (MoS_2, $MoSe_2$, WS_2 and WSe_2) memory (**Figure 21**), which scales to a sub-nanometer [23]. New device concepts in nonvolatile flexible memory and brain-like (neuromorphic) computing can significantly benefit from the tremendous possibilities for designing

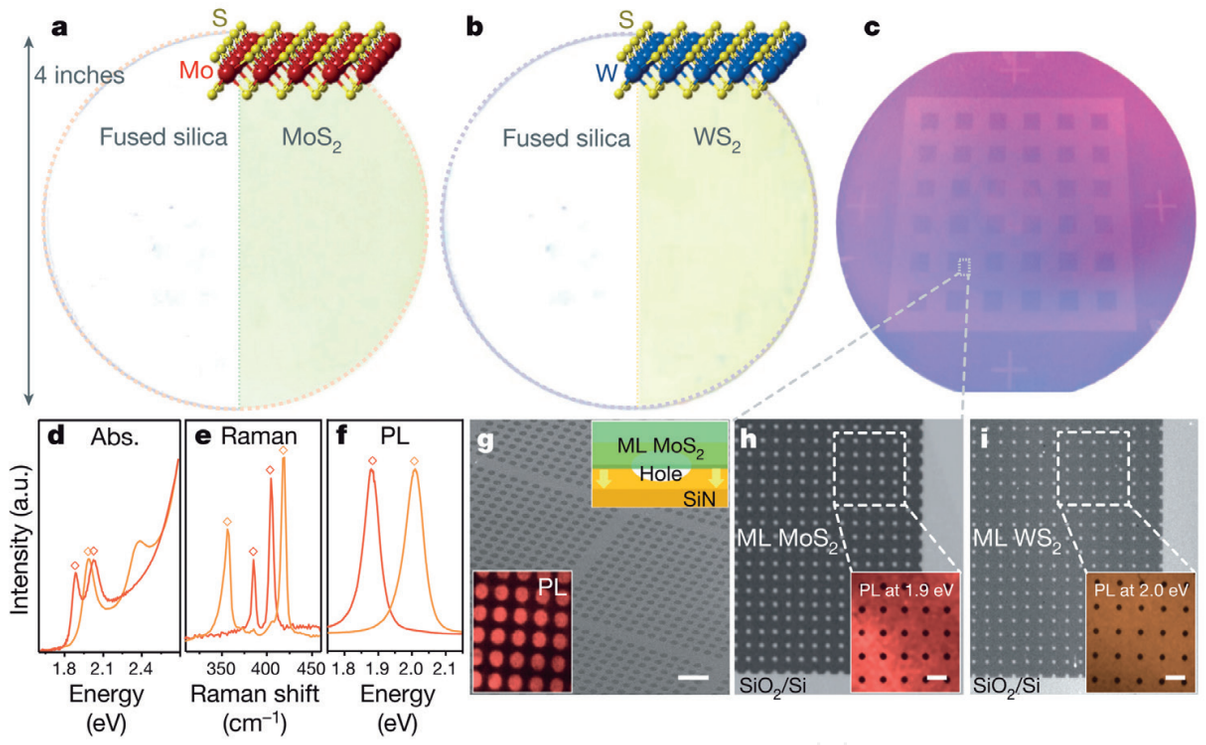

Figure 20. Single-layer transition metal dichalcogenides (TMD) films on 4-inch wafers. a, b, photos of MoS_2 (a) and WS_2 (b) monolayers of films grown on 4-inch substrates with diagrams of their respective atomic structures. The left halves show a quartz substrate for comparison. (c) Photo of a patterned monolayer MoS_2 film on a 4-inch SiO_2/Si wafer (the darker areas are covered with MoS_2). (d) Optical absorption spectra of the MOCVD-grown monolayer MoS_2 (red line) and WS_2 (orange line) in the photon energy range from 1.6 to 2.7 eV. (e) The Raman spectra of the grown monolayer MoS_2 and WS_2 normalized to the intensity of the silicon peak. (f) Normalized photoluminescence spectra of monolayers MoS_2 and WS_2 grown. The peak positions in d–f are consistent with the positions of the peaks obtained from the peeled samples (diamonds). (g) SEM image and photoluminescence (PL) (bottom insert, at 1.9 eV) of monolayer (ML) MoS_2 membranes suspended on a SiN TEM mesh with holes of 2 μm (the suspended film scheme is shown in the upper inset). Label, 10 microns. (h), (i) Optical images (normalized to the area of a clean substrate) of the patterned monolayer MoS_2 (h) and WS_2 (i) on SiO_2 taken from films with a wafer-scale pattern. The insets show photoluminescent images for energies of 1.9 eV (h) and 2.0 eV (i). Scale mark, 10 microns [22].

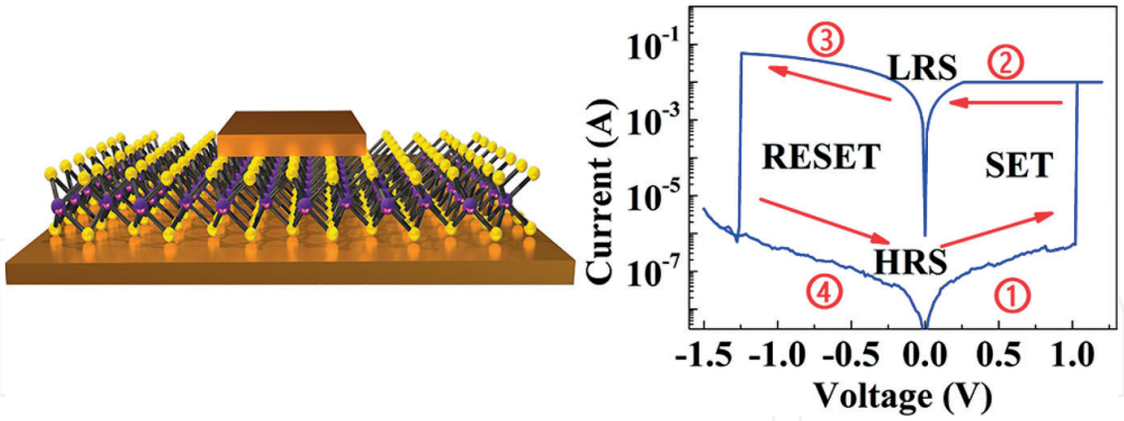

Figure 21. Scheme of a TMD sandwich based on MoS_2 grown on Au foil (left) and a representative curve of I-V behavior of bipolar resistive switching in a MoS_2 monolayer with a lateral area of 2 × 2 μm² (on the right). Step 1: The voltage increases from 0 to 1.2 V. At ~ 1 V, the current rises sharply to the limiting current, indicating the transition (SET) from the high resistance state (HRS) to the low resistance state (LRS). Step 2: The voltage decreases from 1.2 to 0 V. The device remains in the LRS. Step 3: The voltage increases from 0 to 1.5 V. At −1.25 V, the current drastically decreases, indicating a transition (RESET) from LRS to HRS. Step 4: The voltage decreases from −1.5 to 0 V. The device remains in HRS mode until the next cycle [23].

2D materials. A new large application, a static radio frequency (RF) switching, was demonstrated using a MoS_2 monolayer operating at 50 GHz.

Multilayer atomic materials [24] can be used to construct the elemental base of neuromorphic computers. One of the new directions is the creation of solid-state memory of the next generation with phase changes and TMO devices. The devices from 2D crystals have certain advantages in obtaining vertical scaling up to the atomic layer. When replacing metal electrodes with graphene, the entire memory cell can be scaled below 2 nm. In addition, the transparency of graphene and the unique spectroscopic features of 2D materials make it possible to obtain a direct optical characteristic of the device on the production line. At present, manual testing of the device's durability (**Figure 22(a)** and (**b)**) is not enough to meet the requirements for solid-state memory and is a reflection of the emerging state of 2D atomistors in comparison with TMO memories [25]. Through engineering or doping, the durability of the device can be improved, similar to what was observed for amorphous carbon storage devices [26]. Retention of nonvolatile states tested up to a week (**Figure 22(c)**) is already sufficient for certain neuromorphic applications with short-term and medium-term plasticity [27]. The subnanometric thickness of monolayers is promising for the realization of ultrahigh densities. With a free step of 10 nm, the atomic density of 10^{15}/mm³ would provide sufficient space to simulate the density of human synapses (~10^9/mm³) [28]. For a single-bit single-level storage device, this corresponds to a theoretical surface density of 6.4 Tbit/inch².

6.2. High-frequency 2D MoS_2 memristors

Modern switches are implemented using transistor or microelectromechanical devices, both of which are volatile, and the latter also requires a large switching voltage that is not suitable for mobile technologies. Recently, phase change switches have attracted interest [29], but the

requirements for high-temperature phase melting and long switching times have limited their use. 2D memristors offer unprecedented advancement for high-frequency systems due to their low voltage operation, small form-factor, high switching speed and low temperature integration compatible with Si or flexible substrates. Nonvolatile RF switches show promising results with acceptable insertion loss of ~ 1 dB and isolation of >12 dB up to 50 GHz (**Figure 22(d)**). The extracted resistance when the state is On, $R_{ON} \approx 11$ ohms and capacitance when the state is Off, $C_{OFF} \approx 7.7$ fF. This results in a cut-off frequency, which is used to estimate the RF switches (a figure of merit (FOM)) [29, 30] $f_{co} = 1/(2\pi R_{ON} C_{OFF}) \approx 1.8$ THz. Further improvements, especially in terms of scaling, are expected to lead to a significant increase in FOM. A unique combination of independent LRS resistance and area-dependent HRS capacity gives a FOM that can be scaled to 100 s of THz by reducing the area of the device that determines advantages over phase-change switches [29, 30], where the capacitance is proportional to the width, but R_{ON} is inversely dependent, hence, prevents frequency scaling without significant compromise losses. In addition, the high stress of mechanical rupture and the easy integration of 2D materials onto soft substrates enable the production of flexible nonvolatile digital and analog/RF switches capable of withstanding mechanical cycling (**Figure 22(e)**).

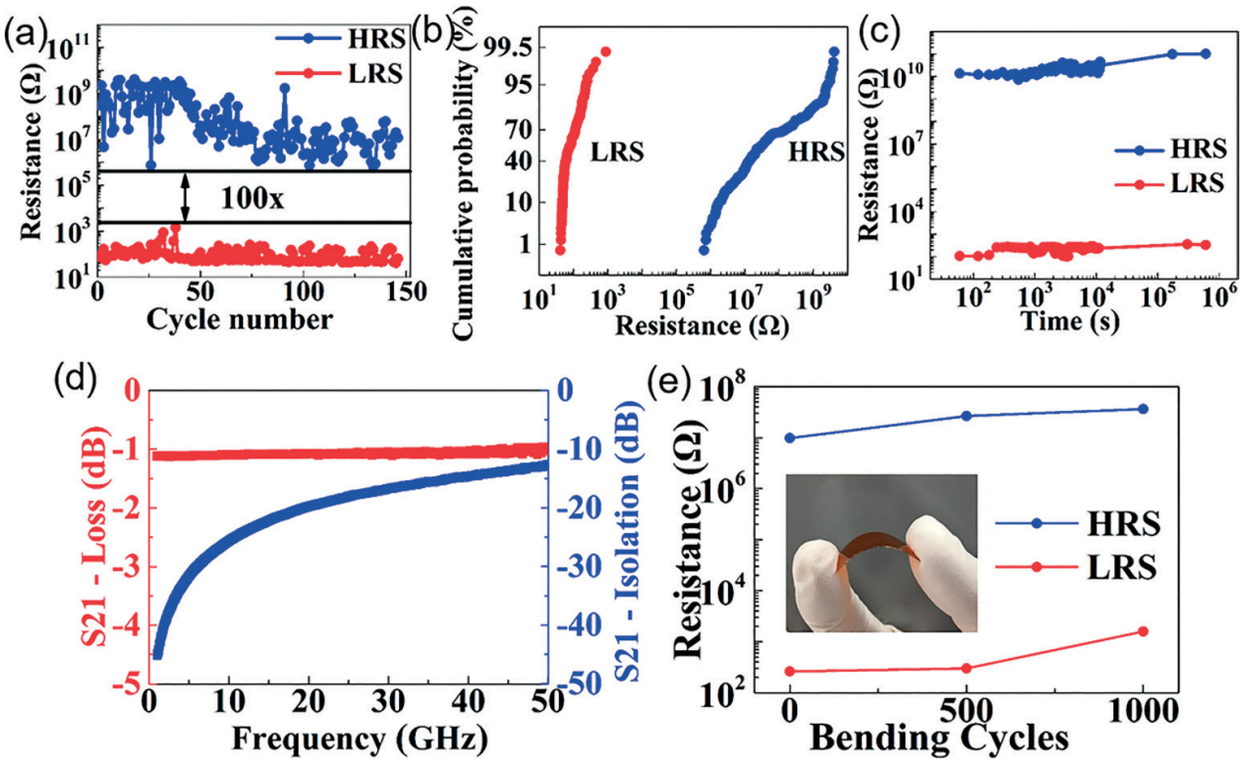

Figure 22. Characteristics of the atomistor. (a, b) Resistance spread of MoS_2 crossbar MIM devices for 150 manual dc switching cycles. (c) Time-dependent measurements of the MoS_2 switch with stable storage of information for a week at room temperature. Resistance of HRS and LRS is determined by measuring the current at a small bias voltage of 0.1 V. The area of this transverse device 2 L-MoS_2 is 2 × 2 μm^2. (d) Experimental, nonvolatile RF switches based on a 1 × 1 μm^2 MoS_2 monolayer show promising characteristics with an insertion loss of ~1 dB and isolation >12 dB up to 50 GHz. The cut-off frequency is ~1.8 THz. (e) Stable resistance of states with high resistance and low resistance after 1000 cycles of bending at 1% strain [23].

7. Conclusion

Memristive systems based on 2D-crystals, a new class of nonvolatile electronic components, are capable of solving the problem of scaling. Self-organized synapse-like memristive systems controlled by transitions between sp^3 and sp^2-configurations of carbon in an electric field can be applied in artificial neural networks and intelligent machines. The high-efficient switching of nonvolatile resistance in atomic single-layer TMD (MoS_2, $MoSe_2$, WS_2, WSe_2) memory is due to the inherent nature of layered crystallinity, which creates clear interfaces and clean tunnel barriers, which prevents excessive leakage and creates stable states. 2D memory can be used for existing applications in the memory/calculation area, as well as in new applications for radio frequency switching with extremely low power consumption. 2D photomemristors with a floating photogate show multiple states controlled in a wide range of electromagnetic radiation and can find application for a wide range of tasks related to neuromorphic computations, image processing and recognition of sounds, movements and speech necessary to create artificial intelligence. The future development of 2D memristive systems should use the possibility of self-organizing technology to form artificial neural networks and hetero-interface interactions of biocompatible 2D crystals, such as graphene, with natural neurons.

Acknowledgements

This research was supported by Basic Science Research Program (2017R1D1A1B03035102) through the National Research Foundation of Korea (NRF) funded by the Ministry of Education, Republic of Korea and by the Russian Foundation of Basic Research (N16-33-60229).

Author details

Gennady N. Panin[1,2]* and Olesya O. Kapitanova[3]

*Address all correspondence to: g_panin@dgu.edu

1 Nano Information Technology Academy, Dongguk University, Seoul, Korea

2 Institute of Microelectronics Technology and High-Purity Materials, Russian Academy of Sciences, Chernogolovka, Moscow, Russia

3 Lomonosov Moscow State University, Leninskie gory, Moscow, Russia

References

[1] Chua LO. Memristor-the missing circuit element. IEEE Transactions on Circuit Theory. 1971;**18**:507-519. DOI: 10.1109/TCT.1971.1083337

[2] Losev OV. Detector-generator; detector-amplifier. Telegraphy and telephony without wires. NRL. 1922;**14**:374-386. (Russ.)

[3] Lossev O. Oscillating crystals. The Wireless World and Radio Review. 1924;**15**:93-96

[4] Bardeen J. Three-electrode circuit element utilizing semiconductive materials. US. Patent No. 2,524,033; Issued October 3, 1950

[5] Bardeen J, Brattain WH. Physical principles involved in transistor action. Physics Review. 1949;**75**:1208-1225. DOI: 10.1103/PhysRev.75.1208

[6] Bardeen J. Semiconductor research leading to the point contact transistor. Nobel Lecture. Science. 1957;**126**:105-112

[7] Shockley W. Semiconductor amplifier. U.S. Patent No. 2,569,347; Issued September 25, 1951

[8] Bardeen J, Brattain WH. The transistor, a semiconductor triode. Physics Review. 1948;**74**: 230-231

[9] Brattain WH, Bardeen J. Nature of the forward current in germanium point contacts. Physics Review. 1948;**74**:231-232

[10] Strukov DB, Snider GS, Stewart DR, Williams RS. The missing memristor found. Nature. 2008;**453**:80-83

[11] Novoselov KS, Geim AK, Morozov SV, Jiang D, Zhang Y, Dubonos SV, Grigorieva IV, Firsov AA. Electric field effect in atomically thin carbon films. Science. 2004;**306**:666-669

[12] Panin GN, Kapitanova OO, Lee SW, Baranov AN, Kang TW. Resistive switching in al/graphene oxide/al structure. Japanese Journal of Applied Physics. 2011;**50**:070110. DOI: 10.1143/JJAP.50.070110

[13] Panin GN, Kapitanova OO, Lee SW, Baranov AN, Kang TW. In Abstract of the 2nd International Symposium on Graphene Devices: Technology, Physics and Modeling. Sendai, Japan; 2010

[14] Kapitanova OO, Panin GN, Baranov AN, Kang TW. Synthesis and properties of graphene oxide/graphene nanostructures. Journal of the Korean Physical Society. 2012;**60**:1789-1793

[15] Kapitanova OO, Panin GN, Kononenko OV, Baranov AN, Kang TW. Resistive switching in graphene/graphene oxide/ZnO heterostructures. Journal of the Korean Physical Society. 2014;**64**:1399-1402

[16] Kapitanova OO. Nanostructures with resistive switching based on graphene oxide [PhD thesis]. Moscow: Moscow State University; 2015

[17] Kapitanova OO, Panin GN, Cho HD, Baranov AN, Kang TW. Formation of self-assembled nanoscale graphene/graphene oxide photomemristive heterojunctions using photocatalytic oxidation. Nanotechnology. 2017;**28**:204005

[18] Goldsmith BR, Coroneus JG, Khalap VR, Kane AA, Weiss GA, Collins PG. Conductance-controlled point functionalization of single-walled carbon nanotubes. Science. 2007;**315**:77

[19] Nagareddy VK, Barnes MD, Zipoli F, Lai KT, Alexeev AM, Craciun MF, Wright CD. Multilevel ultrafast flexible nanoscale nonvolatile hybrid graphene oxide–titanium oxide memories. ACS Nano. 2017;**11**:3010-3021. DOI: 10.1021/acsnano.6b08668

[20] Wang W, Panin GN, Fu X, Zhang L, Ilanchezhiyan P, Pelenovich VO, Fu D, Kang TW. MoS_2 memristor with photoresistive switching. Scientific Reports. 2016;**6**:31224. DOI: 10.1038/srep31224

[21] Chen Z, Ríos C, Pernice WHP, Wright CD, Bhaskaran H. On-chip photonic synapse. Science Advances. 2017;**3**:e1700160. DOI: 10.1126/sciadv.1700160

[22] Kang K, Xie S, Huang L, Han Y, Huang PY, Mak KF, Kim CJ, Muller D, Park J. High-mobility three-atom-thick semiconducting films with wafer-scale homogeneity. Nature. 2015;**520**:656-660. DOI: 10.1038/nature14417

[23] Ge R, Wu X, Kim M, Shi J, Sonde S, Tao L, Zhang Y, Lee JC, Akinwande D. Atomristor: Nonvolatile resistance switching in atomic sheets of transition metal dichalcogenides. Nano Letters. 2018;**18**:434-441. DOI: 10.1021/acs.nanolett.7b04342

[24] Akinwande D, Petrone N, Hone J. Two-dimensional flexible nanoelectronics. Nature Communications. 2014;**5**:5678

[25] Wong H-SP, Lee H-Y, Yu S, Chen Y-S, Wu Y, Chen P-S, Lee B, Chen FT, Tsai M-J. Metal-oxide RRAM. Proceedings of the IEEE. 2012;**100**:1951-1970

[26] Santini CA, Sebastian A, Marchiori C, Jonnalagadda VP, Dellmann L, Koelmans WW, Rossell MD, Rossel CP, Eleftheriou E. Oxygenated amorphous carbon for resistive memory applications. Nature Communications. 2015;**6**:8600

[27] Indiveri G, Liu SC. Liu SC. Memory and information processing in neuromorphic systems. Proceedings of the IEEE. 2015;**103**:1379-1397

[28] Yu S, Kuzum D, Wong HSP. Design considerations of synaptic device for neuromorphic computing. In: 2014 IEEE International Symposium on Circuits and Systems (ISCAS); IEEE; June 1-5, 2014. pp. 1062-1065

[29] Wang M, Rais-Zadeh M. Development and evaluation of germanium telluride phase change material based ohmic switches for RF applications. Journal of Micromechanics and Microengineering. 2017;**27**:013001

[30] Moon JS, Hwa-Chang S, Le D, Helen F, Schmitz A, Oh T, Kim S, Kyung-Ah S, Zehnder D, Baohua Y. 11 THz figure-of-merit phase-change RF switches for reconfigurable wireless front-ends. In: 2015 IEEE MTT-S International Microwave Symposium; IEEE; May 17–22, 2015; pp. 1-4